Synthetic control over the energy transfer and charge transfer between carbon dots and covalent organic framework

IOP Publishing J. Phys. Energy 6 (2024) 025018 https://doi.org/10.1088/2515-7655/ad3677

Journal of Physics: Energy

OPEN ACCESS

RECEIVED
26 November 2023

REVISED
7 March 2024

ACCEPTED FOR PUBLICATION
21 March 2024

PUBLISHED
4 April 2024

PAPER

Synthetic control over the energy transfer and charge transfer between carbon dots and covalent organic framework

Julian Feijoo, Klaudija Paliušytė and Jenny Schneider*

Department of Chemistry and Center for NanoScience, Ludwig-Maximilians-Universität (LMU) München, Butenandtstraße 5-13, 81377 Munich, Germany

* Author to whom any correspondence should be addressed.

E-mail: jenny.schneider@lmu.de

Keywords: carbon dots, covalent organic frameworks, charge transfer, energy transfer, sensing, photocatalysis

Supplementary material for this article is available online

Abstract

Carbon dots (CDs) are environmentally benign, strongly photoluminescent, metal free nanoparticles. Interfacing them with tailor-made organic semiconductors possesing an ordered channel structure such as covalent organic frameworks (COFs) promises to yield multifunctional materials. In this study, microwave-derived CDs are successfully incorporated into the porous structure of COF in a one-pot synthesis in which the condensation reaction between benzo[1,2-b:4,5-b′]dithiophene-2,6-dicarboxaldehyde (BDT) and 1,1,2,2-tetra(p-aminophenyl) ethylene (ETTA) is conducted in the presence of CDs. A detailed structural and optoelectronic characterization of the COF/CDs composite reveals that upon tuning the CDs loadings encapsulated in COF the interaction between both components can be controlled allowing the switch between energy and charge transfer. At CDs loadings $\leqslant$20 wt%, strong binding of CDs to the COF enables charge transfer evinced from the quenched photoluminescence (PL) of both components and accelerated exciton decay kinetics of the COF. At CDs loadings $\geqslant$30 wt% Förster resonance energy transfer from CDs to COF prevails, leading to enhanced COF PL. Our study underlines the interaction mechanism in organic composites and provides the knowledge required for the design of novel functional materials with applications in photocatalysis, optoelectronics and sensing.

1. Introduction

For a long time, inorganic semiconductors were at the forefront of the functional materials for energy and sensing applications. Since then, the focus of the search for cheap materials that can be produced *via* simple modular construction has shifted toward organic materials [1]. In acknowledgment of these materials, the 2000 Nobel Prize in Chemistry was jointly awarded to Heeger, MacDiarmid and Shirakawa for the discovery of conducting polymers. Recently, a new class of organic semiconductors, namely, covalent organic frameworks (COFs), has emerged [2, 3]. COFs are built by rigid organic building blocks that are covalently connected *via* various reversible reactions, *e.g.* imine condensation [4] or Knoevenagel condensation [5]. By rational selection of the building block's symmetry, three-dimensional or two-dimensional (2D) frameworks featuring long-range order and porosity are formed. In addition to their modular structure, COFs are tailor-made materials from the perspective of chemical and physical properties. COFs with specific properties can be designed by installing reactive functional groups or semiconducting organic segments into the building blocks. An intriguing structural property of 2D COFs is their defined, uniform and continuous channels in which guest molecules or particles can be embedded and thus providing a platform for the formation of multifunctional composites.

In this regard, carbon dots (CDs) are an intriguing option [6]. These nanoparticles are made up entirely of abundant, environmentally friendly elements—usually carbon, oxygen, hydrogen and nitrogen—with a

wide spectrum of possible applications ranging from optoelectronics, photocatalysis, biomedical imaging, and sensing [7]. The design of the composite materials based on COF and CDs has attracted a lot of attention since by combining two materials with highly tunable properties countless promising applications can be envisioned. Herein, the interactions between the COF and CDs determine the final functionality of the composite. COFs usually have weak emission because of π–π stacking between layers and intramolecular bond rotation [8, 9]. Encapsulation of the CDs in the COF's porous structure can lead to an enhanced emission yield of the COF *via* energy transfer from CDs to COF. Ma *et al* showed that when the emission spectra of CDs overlap with the absorption spectra of the COF, Förster resonance energy transfer (FRET) occurs resulting in a strong COF photoluminescence (PL) [10]. The PL was dynamically quenched in the presence of Cu^{2+}, allowing the sensitive detection of this metal. Song *et al* prepared a similar system that allowed the detection of Fe^{3+} and Cu^{2+} [11, 12]. Cui *et al* developed an aptasensor employing COF and CDs [13]. The CDs were non-covalently bound to COF and their PL were quenched due to energy transfer to COF. The presence of a certain biomolecule causes the detachment of CDs from the surface and recovery of their original emission. In the case of strong interactions between COF and CDs charge transfer (CT) at the interface of the composite might occur thus suppressing the undesired recombination of the photogenerated charge carriers. Interactions involving CT are crucial in the photocatalytic and optoelectronic applications. Liang *et al* reported the construction of the COF/CDs composite promoting high-flux CT and efficient photocatalytic activity for antibacterial photocatalytic therapy [14]. Zhong *et al* reported COF/CDs composite system for efficient photocatalytic CO_2 to CO reduction [15]. Although the proof of principle for CT and FRET in COF/CDs composites has been demonstrated the control over these two processes *via* the concentration of embedded CDs in COF has not been yet reported.

In this study, a 2D COF constructed from 1,1,2,2-tetra(p-aminophenyl)ethylene (ETTA) and benzo[1,2-b:4,5-b′]dithiophene-2,6-dicarboxaldehyde (BDT) is combined with CDs synthesized by a simple and quick microwave approach. BDT–ETTA COF exhibits suitable features for the studies on energy and charge transfer in COF/CDs composite. BDT–ETTA COF possesses high crystallinity and porosity, PL and efficient charge separation due to the acceptor and donor character of the ETTA and BDT units, respectively, so that the charge transport to CDs can compete with the recombination [16]. CDs synthesized from citric acid (CA) and branched polyethylenimine (BPEI) have previously shown both photocatalytic activity and strong luminescence [17]. Detailed spectroscopic and structural analysis reveals that the energetic interactions between COF and CDs depend on the structural arrangement of the composite, which was controlled *via* adjusting the CDs loading.

2. Methods

2.1. Synthesis of CDs

The CDs were synthesized according to the literature reports [17, 18]. A BPEI purchased from Sigma-Aldrich and anhydrous CA purchased from Merck served as precursors for the CDs synthesis. Herein, CA (1 g) and BPEI (2 g) were dissolved in 20 ml of milli-Q water and stirred at 60 °C for 10 min. The volume was adjusted to 50 ml with water and transferred to the microwave reactor. The sample was then heated at 190 °C for 30 min. The maximum heating rate was set to 900 W. The resulting yellow solution was purified by centrifugation at 25 000 RCF, followed by filtering through a 0.2 μm pore size syringe filter, and freeze drying. The obtained brownish powder was ground with pestle and mortar before use in the COF synthesis.

2.2. Synthesis of BDT–ETTA COF and COF/CDs composite

2.2.1. Synthesis of ETTA

1,1,2,2-Tetraphenylethylene (3.0 g, 9.0 mmol) was slowly added with stirring at 0 °C to a mixture of 30 ml nitric acid ($\geqslant$99%) and 30 ml glacial acetic acid followed by stirring for three hours at room temperature. Then the solution was diluted with cold water. The resulting precipitate was filtered and dried under reduced pressure. Recrystallization from 1,4-dioxane, filtration and drying resulted in a yellow solid of 1,1,2,2-tetra(p-nitrophenyl)ethylene (TNPE) with 69% yield [19]. 1H NMR (400 MHz, $CDCl_3$) δ (ppm): 8.055–8.100 (m, 8H), 7.16–7.21 (m, 8H).

20 ml of anhydrous tetrahydrofuran (THF) was used to dissolve TNPE (1.0 g, 1.9 mmol) under nitrogen atmosphere. Under further stirring 4 g of Raney-nickel catalyst slurry was added [20]. Followed by the dropwise addition of hydrazine monohydrate (1.3 ml, 26 mmol) to the mixture. The mixture was heated to reflux for 2 h. After cooling to room temperature and filtration, the filtrate was dried under reduced pressure leading to a yellow solid of ETTA with 79% yield. 1H NMR (400 MHz, DMSO-d6) δ (ppm): 6.60–6.55 (m, 8H), 6.29–6.24 (m, 8H), 4.84 (s, 8H).

2.2.2. Synthesis of BDT

The synthesis of BDT was adapted from [21]. Herein, benzo[1,2-b:4,5-b′]dithiophene (1.0 g, 5.3 mmol) was dissolved in 100 ml anhydrous THF in an outgassed flask under nitrogen atmosphere. The cooling to −78 °C of the stirred mixture was conducted in a dry ice/acetone cooling bath. A solution of n-butyl lithium (5.0 ml, 2.5 M in n-hexane, 12.5 mmol) was added dropwise within 10 min. Stirring for 30 min at −78 °C and then for 1 h at room temperature were performed. The cooling to −78 °C was repeated followed by the dropwise addition of dimethylformamid (DMF) (1.0 ml, 13.0 mmol) and stirring overnight. The solution was then transferred into ice water and filtered. The yellow precipitate was washed with water several times and further treated with MeOH and Et_2O. The solid was dried under reduced pressure leading to a yellow solid of BDT with 46% yield. 1H NMR (400 MHz, DMSO-d6) δ (ppm): 8.53 (s, 2H), 8.89 (s, 2H), 10.20 (s, 2H).

2.2.3. Synthesis of BDT–ETTA COF and COF/CDs composite

BDT (4.94 mg, 0.0201 mmol), ETTA (3.94 mg, 0.0100 mmol) and CDs (between 0 and 17.76 mg) were added to a culture tube. Benzyl alcohol and mesitylene (V/V 9:1, 500 μl) were added. The mixture was mixed with a pipette before adding acetic acid (6 M, 50 μl). The tube was sealed and kept at 120 °C for 3 d. The resulting precipitate was filtered, washed and extracted with THF.

2.3. Powder x-ray diffraction

Powder x-ray diffraction measurements were performed on a Bruker D8 Discover with Ni-filtered Cu-Kα radiation and a LynxEye position-sensitive detector (scan speed of 4 s per 0.01 degree 2θ).

2.4. Physisorption

Nitrogen sorption isotherms were recorded on a Quantachrome Autosorb 1 at 77 K within a pressure range of $p/p_0 = 0.001$–0.98. Prior to the measurement of the sorption isotherms the samples were heated for 24 h at 120 °C under turbo-pumped vacuum. For evaluating of the surface area the BET model was applied between 0.05 and 0.2 p/p_0. Pore size distributions were calculated using the Quenched Solid Density Functional Theory (QSDFT) equilibrium model (desorption branch) with a carbon kernel for cylindrical pores.

2.5. UV–Vis spectroscopy

UV–Vis spectra were recorded using a Perkin–Elmer Lambda 1050 spectrometer equipped with a 150 mm integrating sphere. For powder measurements $BaSO_4$ was applied as a reference.

2.6. Steady-state and time-resolved PL measurements

PL and PL anisotropy measurements were performed with a FluoTime 300 from PicoQuant GmbH. The samples were photo-excited using a laser with a wavelength of 378 nm (LDH-P-C-375 from PicoQuant GmbH) and 510 nm (LDH-P-C510 from PicoQuant GmbH) pulsed at 500 kHz, with a pulse duration of ∼100 ps and fluence of ∼300 μJ cm^{-2} per pulse. The PL was collected using a high-resolution monochromator and photomultiplier detector assembly (PMAC 192-N-M, PicoQuant GmbH).

2.7. Cyclic voltammetry

Electrochemistry measurements were recorded using 0.1 M NBu_4PF_6 (Aldrich, 99.9%) in acetonitrile (Aldrich, anhydrous) as the electrolyte. The cell was assembled in an argon-filled glove box ($c(O_2) < 0.1$ ppm, $c(H_2O) < 0.1$ ppm). A silver wire served as a reference electrode, that had been kept in concentrated hydrochloric acid for half an hour. Ferrocene potential versus the silver electrode was established to be 440 mV (see figure S1). CDs were measured as a solution, using indium tin oxide (ITO) substrate as a working electrode. When measuring COF thin films, the films themselves were used as the working electrodes. Platinum wire served as the counter electrode. A Metrohm Autolab PGStat302N was used for the measurements.

3. Results

This study aimed to design a multifunctional COF/CDs composite material with structural control over their optoelectronic interactions. For the synthesis of CDs, the microwave approach reported in [17] was adapted. Herein, CA and BPEI were treated in a microwave at 200 °C and under pressure of 20 mbar. Powder x-ray diffractograms (PXRDs) of the obtained CDs (figure 1(a)) show two very broad, overlapping reflections extending from approximately 5–25 2θ. Liang *et al* reported a similar broad reflection for the CDs prepared by condensing CA and ethylenediamine using a hydrothermal method [14]. The broad PXRD reflection indicates low graphitization of the sample. The CDs were further subjected to calcination in an oven at 200 °C and 350 °C. The samples are referred as CDs_150 °C and CDs_200 °C. For both samples reflection at

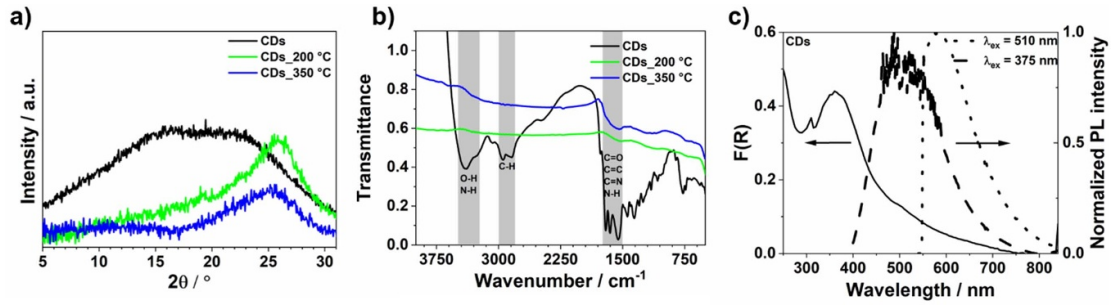

Figure 1. (a) PXRD diffraction patterns and (b) FT-IR spectra (prominent features are highlighted in gray) of untreated CDs (black) and after calcination at 200 °C (green) and 350 °C (blue). (c) $F(R)$ spectrum and PL spectra (at $\lambda_{ex} = 375$ nm (dashes) and at $\lambda_{ex} = 510$ nm (dots)) of untreated CDs.

27 2θ occurred, as shown in figure 1(a), indicating the formation of crystalline particles with a lattice spacing similar to that of graphite [22, 23].

For the quantification of the particle size, the diffractograms were fitted with multiple Gaussian functions to extract FWHM values required for the calculation of the crystallite size *via* the Scherrer equation. The function closest to 27 2θ was selected to obtain the size of graphitic domains. The fits are shown in figure S2 and all relevant values obtained from the fits and the calculated using the Scherrer equation are given in table S1. In the case of the untreated CDs, the center of the Gaussian function is not at 27 2θ in contrast to the tempered CDs. Hence, to estimate the particle size of the CDs PL anisotropy measurements were performed [24, 25]. This method applies the Einstein–Stokes relationship to calculate the hydrodynamic diameter. Herein, the depolarization of the PL is related to the Brownian motion of the particles, which in turn is related to the size of the particles. The fitting is presented in the figure S3. The particle diameters of the tempered CDs obtained from the Scherrer equation and the PL anisotropy are similar, being 1.9 nm for CDs_200 °C, and 2.3 nm for CDs_350 °C. For untreated CDs, only PL anisotropy allowed the accurate particle size quantification of 2.5 nm.

The surface functionality of the CDs was characterized by means of Fourier transformation-infrared spectroscopy (FT-IR) spectroscopy. The FT-IR spectra of the precursors are presented in figure S4 and the corresponding signal assignments in table S2. Figure 1(b) shows the FT-IR spectra of untreated and tempered CDs. Measurements were carried out in transmission on pellets containing the samples and KBr. Untreated CDs show a broad signal at around 3400 cm^{-1} with a shoulder at lower frequencies, which belongs to O–H and N–H stretching vibrations, respectively [17, 26]. This evinces the presence of alcohol and amine groups. The doublet band at around 2950 and 2850 cm^{-1} has previously been assigned to alkyl C–H bond stretching vibration, indicating the presence of sp^3 carbon domains [27]. In addition, there are many absorption bands in the fingerprint region below 2000 cm^{-1}. Most prominently, bands at around 1700 cm^{-1}, 1650 cm^{-1} and 1550 cm^{-1} are associated with C=O, C=C and C=N stretches, as well as with N–H bending [17, 27]. After calcination at 200 °C and 350 °C most IR bands disappeared evincing the loss of the surface functionalization. Although untreated CDs have low crystallinity they possess the suitable size and surface functionalization for the planned incorporation into the porous structure of the COF. Further in-depth characterization is presented for untreated CDs denoted as CDs.

One of the most prominent properties of CDs is their strong PL. UV–Vis and PL spectra of the precursors differ from the spectra of CDs as presented in figure S5. The recorded diffuse reflectance UV–Vis and PL spectra of CDs powder are shown in figure 1(c). The measured UV–Vis reflectance was converted into the Kubelka–Munk function which is proportional to the absorption according to the following equations [28]:

$$F(R) = \frac{(1 - R(\lambda))^2}{2R(\lambda)} = \frac{\alpha(\lambda)}{S(\lambda)} \quad (1)$$

where $F(R)$, $R(\lambda)$, $\alpha(\lambda)$ and $S(\lambda)$ are the Kubelka–Munk function, reflectance referred to $BaSO_4$ standard, absorption coefficient and scattering coefficient at each wavelength, respectively. Apart from an absorption below 300 nm there is a prominent absorption band at 360 nm, as well as a weak shoulder at around 500 nm. The features in the visible wavelength range were previously shown to be caused by different polycyclic aromatic hydrocarbons [29]. Specifically, this involves π–π^* transitions of C=C bonds and n–π^* transitions of C=O groups [26, 30]. The bandgap energy was estimated to be 2.80 eV by means of the Tauc method, as shown in figure S6. When exciting CDs at $\lambda_{ex} = 375$ nm, a broad and intense PL band centered at around 500 nm with a long tail toward longer wavelengths is observed. The large stokes-shift of around 160 nm is due

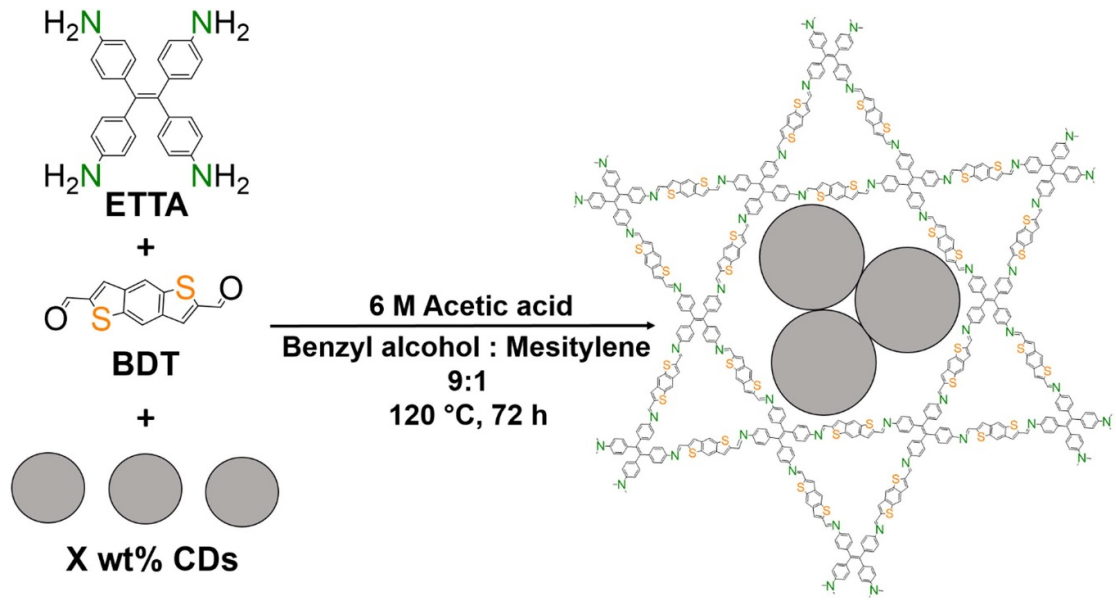

Scheme 1. Schematic representation of the BDT–ETTA COF synthesis in the presence of CDs, *X* was varied between 0 and 100 wt%. Note: the exact position of the CDs within the COF structure is not known.

to exciton self-trapping in the form of excimer formation [29]. The tail toward longer wavelengths has been previously explained by the energy transfer between different chromophores within the CDs. Upon excitation at $\lambda_{ex} = 510$ nm, a less intense PL band is observed with a maximum at around 570 nm. This excitation-dependent emission is a characteristic feature of CDs [30]. This is often ascribed to the multichromophoric nature of CDs which comprises different molecular species as well as defects and surface states [26].

For the synthesis of the COF functionalized with CDs, BDT–ETTA COF was selected. BDT–ETTA was synthesized solvothermally according to a literature report [31]. The appearance of an intense (100) reflection as well as several higher order reflections in the diffractogram confirm the successful formation of the COF (figure 2(a)). The obtained structure of BDT–ETTA-COF is in a good agreement with the simulated a dual-pore Kagome structure in P6 symmetry (see figure S7). The inset of the figure 2(a) shows a magnification of the smaller reflections at slightly higher angles, including the stacking reflection at around 20 2θ which corresponds to a π–π stacking distance of 0.44 nm. For the preparation of COF/CDs composite BDT–ETTA COF was synthesized in the presence of CDs (scheme 1). This approach allows the linkers to be arranged around the CDs as the COF grows. PXRDs demonstrate high crystallinity of samples with up to 20 wt% CDs loadings, as shown in figure 2(a). Less intense higher order reflections can be observed up to 50 wt% loadings, although relative intensities decrease significantly above CDs loading of 20 wt%. Stacking reflection is present for samples with CDs loadings up to 20 wt%, whereas for higher CDs loadings broad reflections at these angles are caused by the presence of CDs.

Nitrogen sorption measurements were conducted to confirm the formation of a porous COF structure and to monitor the changes upon CDs loading. The isotherms and the corresponding pore size distribution (PSD) are shown in figures 2(b) and (d), respectively. For BDT–ETTA COF two sharp volume increases in the isotherm were observed, corresponding to pore sizes of 1.8 and 3.6 nm which belong to the trigonal and hexagonal cavities of the Kagome structure, respectively. The surface area and pore volume were found to be around 1360 $m^2\ g^{-1}$ and 1.2 $cm^3\ g^{-1}$, respectively. Composites with up to 20 wt% CDs loadings show similar behavior with two maxima at about 1.8 nm and 3.6 nm, as expected of a Kagome structure. However, both pore volume and surface area increase with increasing CDs loading, without any change in the shape of the PSD. In contrast, the pore structure of the 100 wt% sample changes significantly, along with a drastic decrease in pore volume and surface area. CDs exhibit no porosity.

Scanning electron microscopy micrographs of the BDT–ETTA COF synthesized in the presence of 0 wt%, 30 wt% and 100 wt% CDs loadings revealed that the morphology of the BDT–ETTA COF changes from the closely packed distinct particles (0 wt%) to less-defined agglomerates as CDs loading increases (figure S8). These morphological changes are consistent with the PXRD data shown in figure 2(a). The transmission electron microscopy image shown in figure S9(a) reveals a high degree of crystallinity and order for pristine BDT–ETTA COF. For the composite containing 30 wt% CDs loading crystalline areas among amorphous areas could be detected as presented in figure S9(b). However, no CDs could be detected most likely due to the small dimensions (around 2 nm), low *Z*-contrast (made up entirely of C, N, O, H), and low crystallinity.

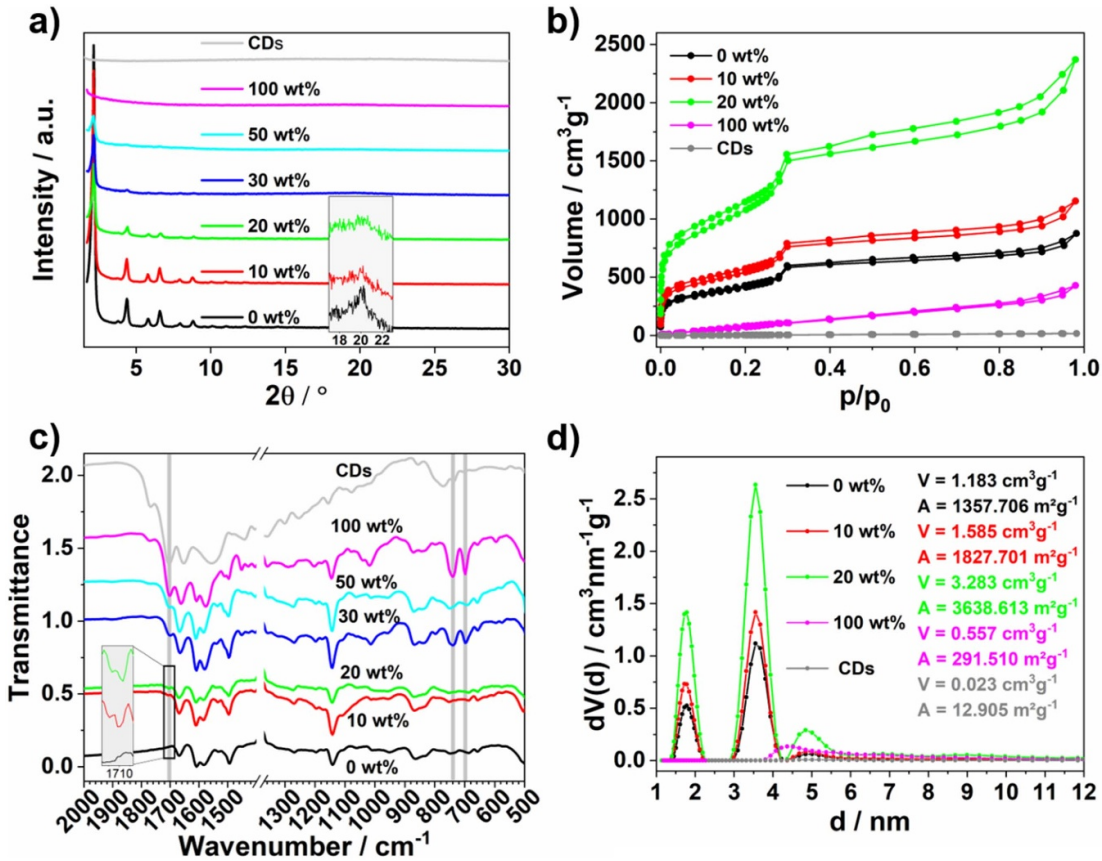

Figure 2. (a) PXRD diffraction patterns with inset showing the stacking peak for the samples with high crystallinity, (b) nitrogen sorption isotherms, (d) calculated PSD, (c) FT-IR-spectra with gray highlighted bands of BDT–ETTA COF synthesized in the presence of different CDs loadings: 0 wt% (black) 10 wt% (red), 20 wt% (green), 30 wt% (blue), 50 wt% (turquoise), 50 wt% (pink), and CDs (gray).

To prove the incorporation of the CDs into the porous structure of the COF and to study the interaction in the composite on the molecular level the FT-IR measurements were conducted (figure 2(c)). The observed FT-IR band at 1668 cm^{-1} in the pristine COF, which is still visible in all COF/CDs composites, can be assigned to the imine-bond [32]. This indicates that the COF layers remain intact in the presence of the CDs loadings up to 100 wt%. The decreased crystallinity for COF samples with high CDs loadings observed in PXRD is a result of less ordered layer stacking [33]. Further changes in FT-IR spectra can be observed as the CDs loading increases. The corresponding sections of the spectra are highlighted in gray. New, weak bands appear at 1780 cm^{-1}, 1700 cm^{-1} and 1360 cm^{-1}, which closely match the bands observed in the pristine CDs. As shown in the inset, the appearance of the signal at 1700 cm^{-1} is observable for samples with low CDs loadings. The presence of CDs features in the COF spectra confirms the co-existence of CDs and COF. However, no shift or appearance of the new FT-IR bands were observed, which excludes the possibility of the covalent bond formation between COF and CDs.

For the additional characterization of the pristine BDT–ETTA COF and of the corresponding composites with CDs elemental analysis was performed. The corresponding data are presented in the table 1. Such elements as C, N, H exist in both components of the composite while S is only present in the BDT unit of the COF and not in CDs. Hence, a gradual decline of S with increasing CDs:COF ratio and an increase of the C and N in the composites compared to the pristine BDT–ETTA COF evince the successful incorporation of the CDs into the COF structure.

For the investigations of the optoelectronic interactions between COF and CDs the UV–Vis diffuse reflectance and PL measurements were conducted on powders. Compared to the building blocks, ETTA and BDT (figure S10), the absorption of the COF is red-shifted as a result of conjugation between the molecular units (figure 3(a)). The bandgap energy of the pristine BDT–ETTA COF was determined *via* the Tauc plot method being 2.09 eV. The Tauc plot is shown in figure S11(a). Upon increasing CDs loading, the color of the COF changes gradually from bright orange to brown. The $F(R)$ spectra shown in figure 3(a) reveal an increase in absorbance in the wavelength range between 600 and 750 nm as the CDs loading increases from 0 to 100 wt%. Furthermore, the absorption onset in the wavelength region between 400 nm and 700 nm shows

Table 1. Material composition obtained from theoretical calculations of BDT–ETTA COF and from elemental analysis of pristine BDT–ETTA COF and BDT–ETTA/CDs composites.

BDT–ETTA COF/CDs (CDs loading in wt%)	N (%)	C (%)	H (%)	S (%)
0 (from simulations)	6.79	73.76	3.91	15.54
0 (synthesized)	5.49	61.47	3.35	13.04
10	6.47	69.9	4.05	12.76
20	6.09	68.36	4.52	11.85
30	6.31	68.48	4.81	11.97
50	7.19	66.13	4.55	9.96
100	8.89	60.21	4.63	7.82

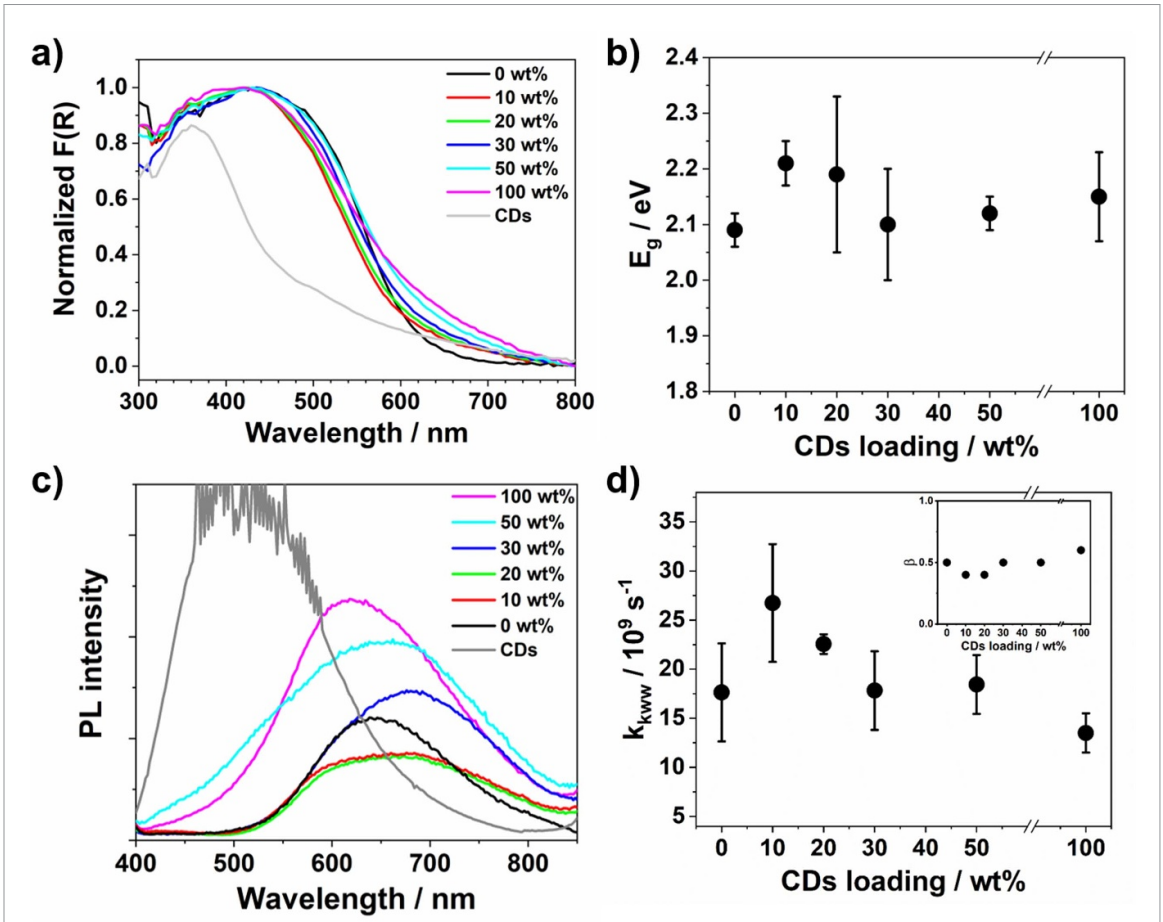

Figure 3. (a) F(R) and (c) PL spectra ($\lambda_{ex} = 375$ nm) of BDT–ETTA COF synthesized in the presence of different CDs loadings: 0 wt% (black) 10 wt% (red), 20 wt% (green), 30 wt% (blue), 50 wt% (turquoise), 50 wt% (pink), and CDs (gray). (b) Optical bandgap energies E_g determined *via* Tauc method and (d) PL decay constants k_{kww} extracted from the stretched exponential fitting according to Kohlrausch–Williams–Watts (KWW) model as a function of CDs loading. (d) The inset shows the distribution breadth β of the decay constant k_{kww}.

a different slope for 100 wt% samples in comparison to the pristine COF. The band gap energies of all samples were determined using the Tauc plot method assuming a direct transition. The corresponding graphs are shown in figure S11. As evident from figure 3(b), E_g does not show any trend with the CDs loading. Figure 3(c) shows the change in the PL of the COF induced by the presence of CDs. For PL spectra, the assumption is made that the penetration depth of the excitation light is less than the thickness of the sample, thus the difference in intensity can be related. Pristine BDT–ETTA COF shows a very broad PL with a maximum at around 690 nm when excited at 375 nm. Compared to the PL spectra of the building blocks shown in figure S12, the formed crystalline COF displays a significant redshift induced by enhanced conjugation. The increase in CDs loading up to 20 wt% leads to a decline in PL intensity of the COF indicating a quenching process. For the CDs loadings higher than 20 wt% the PL intensity of the COF increases gradually with CDs loading. For the samples with CDs loadings from 10 to 50 wt% no shift of the PL maxima occurred, while the sample with 100 wt% shows a blue-shift of the emission. The latter results

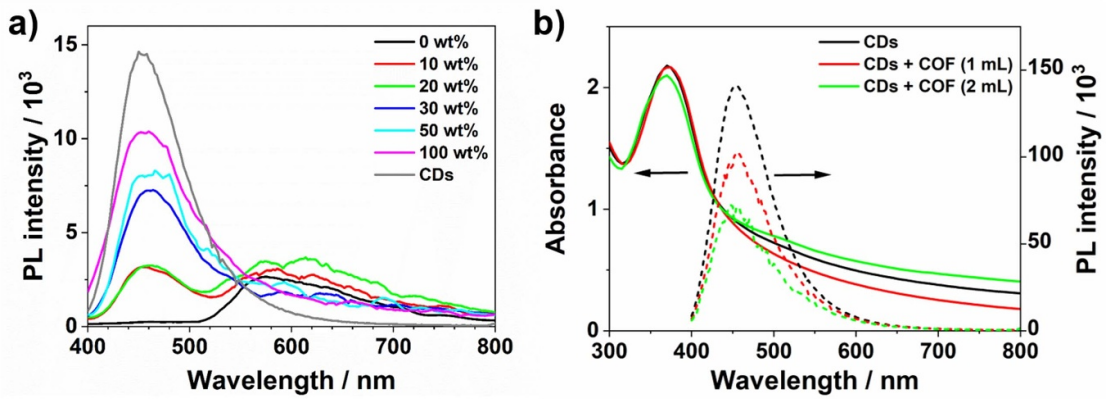

Figure 4. (a) PL spectra of COF suspensions in ACN synthesized in the presence of different CDs loadings: 0 wt% (black) 10 wt% (red), 20 wt% (green), 30 wt% (blue), 50 wt% (turquoise), 50 wt% (pink), and CDs (gray). (b) PL spectra of CDs suspensions in acetonitrile with increasing volume of COF suspension. The total volume was kept constant.

from the loss of crystallinity and thus in conjugation of the COF. The PL spectra of amorphous and crystalline synthesized BDT–ETTA COF are shown in figure S13. The PL band of the CDs is absent in the PL spectra of the composite for all CDs loadings.

Time-resolved PL decays were recorded to identify whether CT between COF and CDs occurs. The observed decay dynamics represent the recombination between photogenerated electron–hole pairs. Due to the low dielectric constant of the COF the electron–hole pair remains bound as an exciton. Hence, it is expected that the decay dynamics follow first order kinetics. However, since the COF contains defects and other irregularities in the structure the photogenerated excitons are not homogeneously distributed in three dimensions. This causes a dispersion of the decay rate constants. The Kohlrausch–Williams–Watts (KWW) model provides mathematical description of the dispersive kinetics. It assumes a Lévy-distribution of first-order rate constants. As shown in equation (2), this results in a stretched-exponential decay of the involved species. Fitting experimental data allows the estimation of the observed rate constant k_r and the distribution width β. From these parameters, the average decay rate constant k_{KWW} is calculated according to equation (3)

$$[A](t) = [A]_0 e^{-(k_r t)^{\beta}} \tag{2}$$

(initial and time dependent concentrations [A](t) and $[A]_0$, observed decay rate constant k_r, time t, distribution breadth β)

$$k_{KWW} = \frac{k_r \beta}{\Gamma\left(\frac{1}{\beta}\right)} \tag{3}$$

(average decay rate constant k_{KWW}, gamma function Γ).

The fitted decays are shown in the figure S14. Figure 3(d) demonstrates that the decay rate constant k_{kww} increases with CDs loadings up to 10 wt% and 20 wt% compared to pristine BDT–ETTA COF, while at loadings of 30 wt% and 50 wt% k_{kww} remains unchanged, and decreases at CDs loading of 100 wt%. Herein, an inverse relationship exists between the decay constants and the PL intensities. The β values presented in the inset of figure 3(d) lie at around 0.5 thus indicating a good agreement between the experimental values and the fitting model.

To gain further insight into the interactions between the COF and CDs mechanical strength was applied to the composite to initiate the separation between the two components. Herein, the samples were treated in acetonitrile by ultrasonication. As opposed to dry powder samples, two distinct PL bands with a maxima at 460 nm and at 580 nm appear in the PL spectra, figure 4(a). The former feature belongs to the PL of CDs while the latter feature belongs to the PL of the BDT–ETTA COF. These results reveal that sonication power causes separation between COF and CDs. The quenching of CDs PL is prevented and the original emission is recovered. Additionally, from figure 4(a) it is evident that CDs PL intensity increases with higher CDs loadings thus revealing that the amount of the CDs embedded in the COF structure increased gradually with the amount of CDs added to the reaction mixture of COF. In further experiment, CDs suspensions of equal concentration were exposed to the different volumes of the COF suspension, herein, the total volume was

kept constant. While the absorbance of CDs did not change as the COF concentration was increased, a gradual decline in the CDs PL intensity with higher COF concentration occurred, see figure 4(b).

4. Discussion

The results presented above allow the construction of a detailed picture of the physicochemical interaction in COF/CDs composite. The appearance of CDs bands alongside the typical COF bands in FT-IR spectra and the elemental analysis confirm the coexistence of the two materials (figure 2(c), table 1). The increased pore volume found in the sorption experiments for the composites up to 20 wt% of CDs loading has already been reported in previous studies and was assigned to the reduction of the interlayer interaction through the insertion of CDs, which transforms the original stacked structure into a thinner 2D-layered structure through self-exfoliation [11]. However, the self-exfoliation is less likely since the PXRD reflections typical for the COF arranged in three dimensions through π–π stacking are still present and are not shifted(figure 2(a)). Additionally, the CDs can act as a diffusion barrier for ETTA and BDT units, leading to slow and controlled growth of the COF. Due to the high surface functionalization, the CDs can also serve as a modulator promoting the growth of the COF. Calik *et al* studied the effect of the modulators on the COF synthesis [34]. The modulator has been found to react reversibly with the COF building blocks thus allowing more controlled growth. The authors observed that addition of small amount of the modulator led to the increased crystallinity, pore volume and surface area of COF-5, which they ascribed to the formation of larger crystallites with few defects. Addition of high modulator concentration, however, resulted in the crystallinity decline. This is well in line with the above presented observations: Samples with CDs loadings of up to 20 wt% showed high crystallinity and increased pore volume and surface area compared to bare COF. On the other hand, CDs loadings of $\geqslant$30 wt% hampered the COF formation leading to loss in crystallinity as shown in figure 2(a)). It can be concluded from the above discussion that the chosen method to obtain the composite via growth of COF in the presence of the CDs has limitations. On the one side, the presence of the functional groups on the surface of the CDs enables the incorporation of the CDs into the porous structure of the COF. On the other side, CDs can impede the crystallization process of the COF resulting in the amorphous product. For example, CDs with their functional groups can act as the COF building block and exchange the linker [35]. Additionally, we have tested different synthetic methods in which COF served as a template for the CDs synthesis, however, the BDT–ETTA COF did not survive the harsh conditions of the synthesis.

The observed structural interactions between BDT–ETTA COF and CDs imposes the evolution of the novel photophysical features which were not present in the single components. The main observations in this regard are: (1) for all CDs loadings the PL band of the CDs disappeared; (2) for CDs loadings $\leqslant$20 wt% a decrease in PL intensity and acceleration of the PL decay rate of functionalized COF compared to pristine COF occurred; (3) for CDs loadings $\geqslant$30 wt% an increase in PL intensity and deceleration of the PL decays of COF compared to pristine COF occurred. The first observation reveals a quenching process of the CDs PL operating either *via* charge or/and energy transfer. The second observation indicates the quenching of the COF PL features *via* CT, while the third observation can originate from the FRET between COF and CDs. To validate these hypotheses, the energetics of the COF and CDs have been analyzed. For an efficient charge transport among the strong structural interaction an alignment of the energetics is required. The energetic positions of the HOMO were determined by cyclic voltammetry from the onset potentials of the oxidative features (figure S15). The position of the LUMO was calculated from the HOMO and the band gap energy. The HOMO and LUMO positions for COF are -5.29 eV and -3.20 eV, respectively, and for CDs -4.96 eV and -2.16 eV, respectively. Accordingly, HOMO and LUMO positions of the CDs are at less negative potentials than those of BDT–ETTA COF. This configuration can result in either a type II or a *Z*-scheme band alignment. In figure 5(a), we have schematically illustrated the type II band alignment: CT can occur via hole transfer from the COF to CDs and electron transfer from CDs to COF. In the case of a *Z*-scheme alignment, an electron from the COF would recombine with a hole from the CDs. In both cases, acceleration of the PL decay through CT will occur as evident from figure 3(d).

For the energy transfer an overlap between the emission of the CDs and the absorption of BDT–ETTA COF is required according to the FRET theory. Apart from the spectral overlap, close proximity of energy donor and energy acceptor, typically on the order of 1–10 nm is needed. Figure 5(b) demonstrates the energetic overlap between COF and CDs. Both CT and FRET will quench the PL of CDs. Most obviously, this was shown by the systematic decrease of the PL of a CDs suspension with increasing COF concentration (figure 4(b)). In the bulk samples, the close association of CDs with COF leads to complete disappearance of CDs PL, substantiating the operation of both CT and FRET. Furthermore, the control experiment, shown in figure 4(a), demonstrates that the CDs did not become a part of the COF as through the application of the external force the CDs were separated from the COF leading to the recovery of its original emission. The emission of COF is quenched only by the CT process at CDs loadings $\leqslant$20 wt%, while FRET causes enhanced

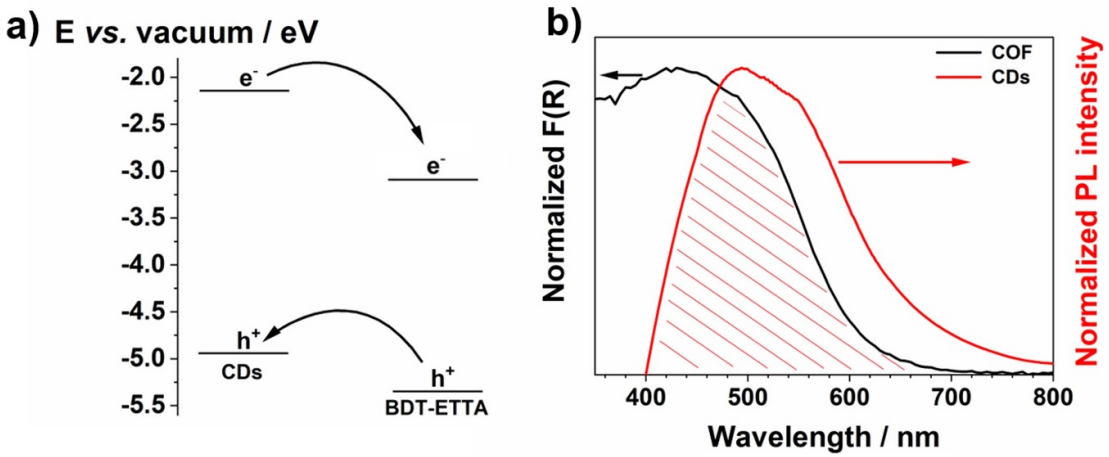

Figure 5. Illustration of the two processes that occur between CDs and BDT–ETTA COF in a corresponding composite: (a) charge transfer and (b) Förster resonance energy transfer.

PL at CDs loadings ⩾30 wt%. The appearance of two different mechanisms dependent on CDs loading can be explained as follows: Stronger contact and interaction between CDs and COF can be assumed at low CDs loading. In that situation, the CT process dominates, leading to complete quenching of PL of CDs, as well as of the COF. As the CDs ratio increases, a thin layer starts to form around the COF crystallites. Once completed, additional CDs cannot directly interact with the COF, but are instead attached to the previous CDs layer. Here, CT is prohibited. However, the CDs meet the spatial distance requirements for FRET to occur. As mentioned before, FRET occurs at the distances between donor and acceptor of up to around 10 nm. As result of FRET, enhanced PL of COF is obtained. FRET from CDs to COF has already been reported [10, 12, 13]. These conclusions are further supported by the kinetic data obtained from the time-resolved PL measurements. The COF decay rate constant increases for 10 and 20 wt% samples as a result of the additional decay pathway *via* CT (see figure 5(a)). At higher loadings, FRET from CDs repopulates the excited state of COF, slowing the overall observed decay. These observations have also been demonstrated by another group [10].

5. Conclusions

COF/CDs composites were successfully prepared by solvothermal synthesis of BDT–ETTA COF in the presence of different CDs concentrations. CDs with their high surface functionalization affect the crystallization process of the COF. For CDs loadings up to 20 wt%, they served as the modulator promoting the growth of the BDT–ETTA COF, while at higher CDs loadings the crystallization of COF was hindered. The incorporation of the CDs into the porous structure of the COF was demonstrated for all CDs loadings by FT-IR spectroscopy. Elemental analysis revealed that the amount of CDs encapsulated in COF increased gradually with the concentration of the CDs present during the COF synthesis. This synthetic control over the COF:CDs ratio in the composite enabled systematic study of the optoelectronic interactions between the two components. Close contact between the two materials at low CDs loadings enabled interfacial CT evinced by the PL quenching of the BDT–ETTA COF and CDs as well as by the acceleration of the PL decay kinetics of COF. At CDs loadings ⩾30 wt%, the contact between both components decreased, however, spatial distance requirements for FRET to occur were fulfilled and the energy transfer prevailed leading to the increased PL of the BDT–ETTA COF. This study demonstrates the structure–property relationship in COF/CDs composites and provides important insights for the applications in photocatalysis and sensing.

Data availability statement

All data that support the findings of this study are included within the article (and any supplementary files).

Acknowledgments

The authors gratefully acknowledge the funding by the LMU Center for NanoScience. J Schneider also acknowledges Alexander von Humboldt Foundation by Return Fellowship Grant. The authors are thankful to Dr Markus Döblinger und Mr Steffen Schmidt for TEM and SEM measurements, respectively.

ORCID iD

Jenny Schneider https://orcid.org/0000-0002-6741-2830

References

[1] Wöhrle D and Meissner D 1991 Organic solar cells *Adv. Mater.* **3** 129
[2] Côté A P, Benin A I, Ockwig N W, O'Keeffe M, Matzger A J and Yaghi O M 2005 Porous, crystalline, covalent organic frameworks *Science* **310** 1166
[3] Lohse M S and Bein T 2018 Covalent organic frameworks: structures, synthesis, and applications *Adv. Funct. Mater.* **28** 1705553
[4] Uribe-Romo F J, Hunt J R, Furukawa H, Klöck C, O'Keeffe M and Yaghi O M 2009 A crystalline imine-linked 3-D porous covalent organic framework *J. Am. Chem. Soc.* **131** 4570
[5] Bi S, Yang C, Zhang W, Xu J, Liu L, Wu D, Wang X, Han Y, Liang Q and Zhang F 2019 Two-dimensional semiconducting covalent organic frameworks via condensation at arylmethyl carbon atoms *Nat. Commun.* **10** 2467
[6] Xu X, Ray R, Gu Y, Ploehn H J, Gearheart L, Raker K and Scrivens W A 2004 Electrophoretic analysis and purification of fluorescent single-walled carbon nanotube fragments *J. Am. Chem. Soc.* **126** 12736
[7] Sciortino A, Cannizzo A and Messina F 2018 Carbon nanodots: a review—from the current understanding of the fundamental photophysics to the full control of the optical response C **4** 67
[8] Gao Q, Li X, Ning G H, Leng K, Tian B, Liu C, Tang W, Xu H S and Loh K P 2018 Highly photoluminescent two-dimensional imine-based covalent organic frameworks for chemical sensing *Chem. Commun.* **54** 2349
[9] Dalapati S, Jin E, Addicoat M, Heine T and Jiang D 2016 Highly emissive covalent organic frameworks *J. Am. Chem. Soc.* **138** 5797
[10] Ma X, Yang Y, Ma R, Zhang Y, Zou X, Zhu S, Ge X, Yuan Y, Zhang W and Zhu G 2020 Inorganic nanocrystal-dynamic porous polymer assemblies with effective energy transfer for sensitive diagnosis of urine copper *Chem. Sci.* **11** 12187
[11] Wang S, Guo L, Chen L, Wang L and Song Y 2022 Self-exfoliating double-emission N-doped carbon dots in covalent organic frameworks for ratiometric fluorescence "off–on" Cu^{2+} detection *ACS Appl. Nano Mater.* **5** 1339
[12] Song Y, Guo L, Du Y, Yang L and Wang L 2020 Dual emission N-doped carbon dot@benzotrithiophene tricarbaldehyde-terephthalic dihydrazide covalent organic framework *Chem. Commun.* **56** 14913
[13] Cui J, Kan L, Li Z, Yang L, Wang M, He L, Lou Y, Xue Y and Zhang Z 2021 Porphyrin-based covalent organic framework as bioplatfrom for detection of vascular endothelial growth factor 165 through fluorescence resonance energy transfer *Talanta* **228** 122060
[14] Liang J, Li W, Chen J, Huang X, Liu Y, Zhang X, Shu W, Lei B and Zhang H 2022 Carbon dots as an electron extractant for enhanced photocatalytic antibacterial activity of covalent organic frameworks *J. Mater. Chem.* A **10** 23384
[15] Zhong H, Sa R, Lv H, Yang S, Yuan D, Wang X and Wang R 2020 Covalent organic framework hosting metalloporphyrin-based carbon dots for visible-light-driven selective CO_2 reduction *Adv. Funct. Mater.* **30** 2002654
[16] Jakowetz A C, Hinrichsen T F, Ascherl L, Sick T, Calik M, Auras F, Medina D D, Friend R H, Rao A and Bein T 2019 Excited-state dynamics in fully conjugated 2D covalent organic frameworks *J. Am. Chem. Soc.* **141** 11565
[17] Bhattacharyya S, Ehrat F, Urban P, Teves R, Wyrwich R, Döblinger M, Feldmann J, Urban A and Stolarczyk J 2017 Effect of nitrogen atom positioning on the trade-off between emissive and photocatalytic properties of carbon dots *Nat. Commun.* **8** 1401
[18] Barman M K, Bhattacharyya S and Patra A 2013 Steady state and time resolved spectroscopic study of C-dots–MEH–PPV polymer nanoparticles composites *Phys. Chem. Chem. Phys.* **15** 16834
[19] Gorvin J H 1959 Polyphenylethylenes. Part I. Preparation and characteristics of Tetra-p-Nitrophenylethylene *J. Chem. Soc.* 678
[20] Lu J and Zhang J 2014 Facile synthesis of azo-linked porous organic frameworks via reductive homocoupling for selective CO_2 capture *J. Mater. Chem.* A **2** 13831
[21] Koßmehl G, Beimling P and Manecke G 1983 Über Polyarylenalkenylene Und Polyheteroarylenalkenylene, 14. Synthesen Und Charakterisierung von Poly(Thieno[2′,3′:1,2]Benzo[4,5-b]Thiophen-2,6-Diylvinylenarylenvinylen)En, Poly(4,8-Dimethoxythieno[2′,3′:1,2]Benzo[4,5-b]Thiophen-2,6-Diylvinylenarylenviny *Makromol. Chem.* **184** 627
[22] Martindale B C M, Hutton G A M, Caputo C A, Prantl S, Godin R, Durrant J R and Reisner E 2017 Enhancing light absorption and charge transfer efficiency in carbon dots through graphitization and core nitrogen doping *Angew. Chem., Int. Ed.* **56** 6459
[23] Peng H and Travas-Sejdic J 2009 Simple aqueous solution route to luminescent carbogenic dots from carbohydrates *Chem. Mater.* **21** 5563
[24] Bruno A, Alfe M, Apicella B, de Lisio C and Minutolo P 2006 Characterization of nanometric carbon materials by time-resolved fluorescence polarization anisotropy *Opt. Lasers Eng.* **44** 732
[25] Chenchiliyan M *et al* 2019 Nanoscale imaging, sensing, and actuation for biomedical applications XVI *Proc. SPIE* **10891**
[26] Bramhaiah K, Bhuyan R, Mandal S, Kar S, Prabhu R, John N S, Gramlich M, Urban A S and Bhattacharyya S 2021 Molecular, aromatic, and amorphous domains of N-carbon dots: leading toward the competitive photoluminescence and photocatalytic properties *J. Phys. Chem.* C **125** 4299
[27] Zhao X, Zhang J, Shi L, Xian M, Dong C and Shuang S 2017 Folic acid-conjugated carbon dots as green fluorescent probes based on cellular targeting imaging for recognizing cancer cells *RSC Adv.* **7** 42159
[28] Kubelka P and Munk F 1931 Ein Beitrag Zur Optik der Farbanstriche *Z. Tech. Phys.* **12** 593
[29] Fu M, Ehrat F, Wang Y, Milowska K Z, Reckmeier C, Rogach A L, Stolarczyk J K, Urban A S and Feldmann J 2015 Carbon dots: a unique fluorescent cocktail of polycyclic aromatic hydrocarbons *Nano Lett.* **15** 6030
[30] Wang Y and Hu A 2014 Carbon quantum dots: synthesis, properties and applications *J. Mater. Chem.* C **2** 6921–39
[31] Sick T *et al* 2018 Oriented films of conjugated 2D covalent organic frameworks as photocathodes for water splitting *J. Am. Chem. Soc.* **140** 2085
[32] Saini A K, Carlin C M and Patterson H H 1993 Confirmation of the presence of imine bonds in thermally cured polyimides *J. Polym. Sci.* A **31** 2751
[33] Sick T *et al* 2019 Switching on and off interlayer correlations and porosity in 2D covalent organic frameworks *J. Am. Chem. Soc.* **141** 12570
[34] Calik M, Sick T, Dogru M, Döblinger M, Datz S, Budde H, Hartschuh A, Auras F and Bein T 2016 From highly crystalline to outer surface-functionalized covalent organic frameworks—A modulation approach *J. Am. Chem. Soc.* **138** 1234
[35] Chen S, Sun T, Zheng M and Xie Z 2020 Carbon dots based nanoscale covalent organic frameworks for photodynamic therapy *Adv. Funct. Mater.* **30** 2004680